

ARTICLE OPEN



Localized corrosion and repassivation behaviors of additively manufactured titanium alloys in simulated biomedical solutions

Dong-Il Seo¹ and Jae-Bong Lee¹✉

The localized corrosion behavior of additively manufactured (AM) titanium alloys is studied based on the relation between pitting potentials, the flux of oxygen vacancies in a passive film, and the repassivation rate using potentiodynamic polarization, Mott–Schottky, and an abrading electrode techniques. The relationship between the localized corrosion resistance and the repassivation behaviors of AM titanium alloys was explained by the survival probability constant based upon the point defect model which describe the generated oxygen vacancies and accumulated cation vacancies affect the occurrence of the localized corrosion. Localized corrosion can be initiated by survival pits under sufficient conditions of the breakdown passive films. Survival probability is constant means a quantitative probability value of the transition from metastable pit to stable pit to occur localized corrosion. The higher the survival probability constant of AM titanium alloys, the more difficult repassivation and the easier occurrence of localized corrosion.

npj Materials Degradation (2023)7:44; <https://doi.org/10.1038/s41529-023-00363-4>

INTRODUCTION

Titanium (Ti) alloys have been used in many fields such as aerospace, marine, and medical industries for many years^{1–3}. This is attributed to their high strength-to-density ratio and excellent corrosion resistance⁴. The outstanding corrosion resistance of Ti alloys is attributed to their protective passive layers on their surface^{5,6}. The biocompatibility of passive films on Ti alloys is an essential factor in human body biomaterials. Commercial pure titanium (CP Ti; α phase) has been used as biomaterials. However, their mechanical strength was not satisfactory in some hard tissues or load-bearing parts. Therefore, $\alpha + \beta$ -type Ti alloys such as Ti–6Al–4V and Ti–6Al–7Nb were developed. Although $\alpha + \beta$ -type Ti alloys have high strength and good fatigue resistance, the containing aluminum (Al) and vanadium (V) elements have the potential problems of Alzheimer's and are toxic to the human body, respectively⁷. Additionally, Young's modulus of $\alpha + \beta$ -type Ti alloys is higher than that of human bones⁸. Hence, the stress-shielding effect may occur because of the difference in Young's modulus between an implant and the bone. Recently, β -type Ti alloys with low modulus for preventing the stress-shielding effect and containing nontoxic elements have been developed such as Ti–13Nb–13Zr (near β) and Ti–15Mo⁹.

Nowadays, additively manufactured (AM) Ti alloys have become popular because of the advantage of their buy-to-fly ratio, which is approximately 1/20 compared with conventional subtractively manufactured (SM) Ti alloys¹⁰. AM processes include several versatile methods such as directed energy deposition (DED), selective laser melting (SLM), and electron beam melting (EBM)^{11,12}. During the DED process, a laser beam generates a molten pool. Powder materials are delivered by argon (Ar) gas and locally injected to fuse and solidify into a bead. DED has a higher degree of freedom in composition design than the other two methods, as it can simultaneously feed powder. Conversely, because SLM and EBM are powder bed fusion processes, metallic powders are uniformly spread on the platforms using a rake, as

distinct from DED. The SLM process can control thinner layers than the DED process, whereas the EBM process generates a faster build rate than the DED process.

From a mechanical perspective, the strength and ductility of AM Ti alloys are comparable with or even greater than those of SM methods^{13–15}. However, AM Ti alloys have lower corrosion resistance than SM Ti alloys due to anisotropy caused by the stacking direction and rapid solidification of the martensite phase^{16,17}. SM Ti alloys (α or $\alpha + \beta$ type) have a microstructure comprising α or $\alpha + \beta$ phases, whereas AM Ti alloys contain martensite α' phases¹⁸. The martensite α' phase is unstable and significantly reduces the corrosion resistance of AM Ti alloys¹⁹. Dai et al.²⁰ studied the corrosion behavior of AM Ti–6Al–4V alloys and found that the higher the proportion of the acicular martensitic α' phase, the weaker the formation of a weaker passive layer. Seo and Lee^{21–23} investigated the uniform and localized corrosion resistance of AM Ti–6Al–4V alloys using potentiodynamic polarization, electrochemical impedance spectroscopy (EIS), electrochemical critical pitting temperature, and electrochemical critical localized corrosion temperature²⁴. They found that the reduction in localized corrosion resistance of AM Ti alloys was caused by the formation of martensite α' phases and their distribution.

Meanwhile, many researchers have investigated the corrosion resistance of SM or AM Ti alloys in terms of the semiconductive properties of passive films^{9,12,25,26}. Chen et al.²⁶ measured the corrosion resistance of passive films formed on AM Ti–6Al–4V alloys in dynamic Hank's solution and explained the corrosion resistance of passive films on AM Ti–6Al–4V alloys using a point defect model (PDM)^{27,28}. In the PDM, a passive film contains several point defects, including oxygen or cation vacancies, which act as donors and acceptors, respectively²⁹. An increase in donor density in the passive film may be attributed to an increase in oxygen vacancies. Thus, Chen et al.²⁶ reported that a higher density of oxygen vacancies and a higher oxygen diffusion coefficient of passive films reduced the corrosion resistance on AM

¹School of Advanced Materials Engineering, Kookmin University, 77 Jeongneung-ro, Seongbuk-gu, Seoul 02707, Republic of Korea. ✉email: leejb@kookmin.ac.kr

Ti–6Al–4V alloys. Gai et al.¹² researched passive films formed on AM or SM Ti–6Al–4V alloys via Mott–Schottky analysis, transmission electron microscopy, and X-ray photoelectron spectroscopy. They found that a high oxygen diffusion coefficient and flux of oxygen vacancies are affected by a decrease in localized corrosion resistance of AM and SM Ti–6Al–4V alloys. Cheng et al.⁹ investigated the corrosion behaviors of Ti–10Mo–6Zr–4Sn–3Nb and Ti–6Al–4V in Hank's solution. They reported that not only a high oxygen diffusion coefficient but also the fast flux of oxygen vacancies of passive films on Ti alloys played an important role in the deterioration of localized corrosion resistance.

Additionally, the repassivation kinetics, which is the rapid recovery after the breakdown of passive films on Ti alloys in biomedical environments, is a critical factor. In the initiation of localized corrosion on passive films, rapid repassivation is indispensable to prevent Ti alloys from further localized corrosion on the human body^{30,31}. Lee and Seo evaluated the localized corrosion resistance of AM Ti alloys using the electrochemical critical localized corrosion potential (E-CLCP) method^{32,33}. E-CLCP is an evaluation method of the localized corrosion resistance of AM Ti alloys by measuring the repassivation potential. This method combines potentiodynamic–galvanostatic–potentiostatic techniques in biomedical environments. Repassivation potential means the possibility that stably growing pit corrosion or crevice corrosion ceases to grow. The repassivation potential of AM Ti alloys in the human body can be used to assess their resistance to localized corrosion.

In this study, the localized corrosion resistance and repassivation behaviors of AM Ti alloys were investigated through various electrochemical tests such as potentiodynamic polarization, EIS, Mott–Schottky techniques, abrading electrode tests, and E-CLCP tests. The relationship between the pitting potential, repassivation rate, and flux of oxygen vacancies in various Ti alloys, such as SM Ti–6Al–4V and AM Ti–6Al–4V, AM Ti–6Al–7Nb, AM CP Ti, and AM Ti–13Nb–13Zr, was examined. Repassivation kinetics was also investigated via E-CLCP and the survival probability constant was calculated from the semiconductive properties of passive films on AM Ti alloys in biomedical environments.

RESULTS AND DISCUSSION

Potentiodynamic polarization studies

Figure 1 shows the potentiodynamic polarization curves of the SM and AM Ti alloys in Ringer solutions at 37 °C. As shown in Fig. 1,

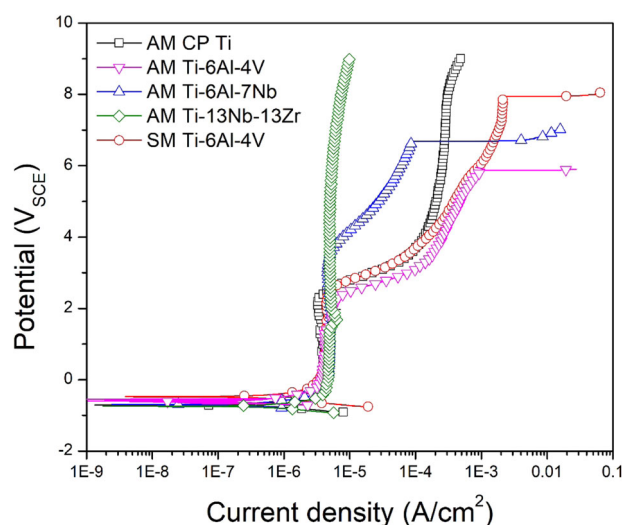


Fig. 1 Potentiodynamic polarization techniques of SM and AM Ti alloys in Ringer solution at 37 °C.

the pitting potentials on AM Ti–6Al–4V, AM Ti–6Al–7Nb, and SM Ti–6Al–4V alloys are represented as 5.83 (± 0.15) V, 6.68 (± 0.18) V, and 7.96 (± 0.45) V, respectively, whereas AM CP Ti and AM Ti–13Nb–13Zr do not exhibit a pitting behavior up to maximum 9V, depending on the substrate. Particularly, the pitting potential of AM Ti–6Al–4V was lower than that of the SM Ti–6Al–4V alloy because of the formation of acicular martensite α' phases^{21–23}.

EIS and Mott–Schottky studies

To determine the film formation potentials, the potentiodynamic polarization tests of SM and AM Ti alloys were conducted. Considering the passive potential region, 1.0, 1.5, and 2.0 V were chosen as the film formation potentials.

Figure 2a–c shows the EIS test results of SM and AM Ti alloys according to the different film formation potentials (1.0, 1.5, and 2.0 V), respectively. A Randles circuit model was used to represent an equivalent circuit with solution resistance (R_s), charge transfer resistance (R_{ct}), and constant phase elements (CPE) of the double layer (CPE_{dl}). CPE implies an imperfect capacitor value deviated from the ideal capacity because of the effect of surface inhomogeneity and roughness. The effective capacitance (C_{eff}) defined in Eq. (1)³⁴ is calculated using R_s and R_{ct} as follows:

$$C_{eff} = \left[Q \left\{ \frac{R_s + R_{ct}}{R_s R_{ct}} \right\}^{(a-1)} \right]^{\frac{1}{a}}, \quad (1)$$

where Q represents the CPE coefficient value and a represents the exponent of CPE ranging from 0 to 1, which is related to the nonuniform current distribution. Hence, a represents the deviation from the ideal capacitor. The ideal capacitor response in the system corresponds to a fitted a value of 1. If the value of a is 0.9 or more, the constant phase element can be regarded as a capacitor.

Capacitance should influence the effective film thickness d_{eff} according to Eq. (2)³⁵.

$$d_{eff} = \frac{\epsilon \epsilon_0}{C_{eff}}, \quad (2)$$

where ϵ represents the dielectric constant of a passive film (considered 85³⁵ in the case of passive films on Ti alloys) and ϵ_0 represents the vacuum permittivity of free space (8.854×10^{-14} F cm⁻¹).

Figure 3a–c shows the Mott–Schottky plots of the passive films formed on the SM and AM Ti alloys at the film formation potentials of 1.0, 1.5, and 2.0 V. The results show the existence of three potential ranges due to the different capacitance behaviors and the n-type semiconductor behaviors of the oxide film of SM, as depicted in the positive slopes of the R2 region. From the slopes in the R2 region shown in Fig. 3a–c, donor densities of SM and AM Ti alloys for n-type semiconductors can be calculated using Eq. (3)^{35,36}.

$$\frac{1}{C_{sc}^2} = \frac{2}{\epsilon \epsilon_0 e N_D} \left(E - E_{fb} - \frac{kT}{e} \right) \text{ for n-type semiconductors,} \quad (3)$$

where e represents the electron charge, N_D denotes the donor density, E_{fb} denotes the flat band potential, k represents the Boltzmann constant, and T represents the absolute temperature. N_D can be determined using the slopes of the Mott–Schottky plots. As shown in Table 1, the calculated donor densities are in order of 10^{18} – 10^{19} . Regardless of the film formation potentials, the calculated donor densities consistently increased in the following order: SM Ti–6Al–4V and AM Ti–6Al–4V, AM Ti–6Al–7Nb, AM CP Ti, and AM Ti–13Nb–13Zr. This is completely different from what we expect, based on pitting potentials.

Abrading electrode studies

To investigate the difference in the localized corrosion resistance between various SM and AM Ti alloys, the repassivation kinetics

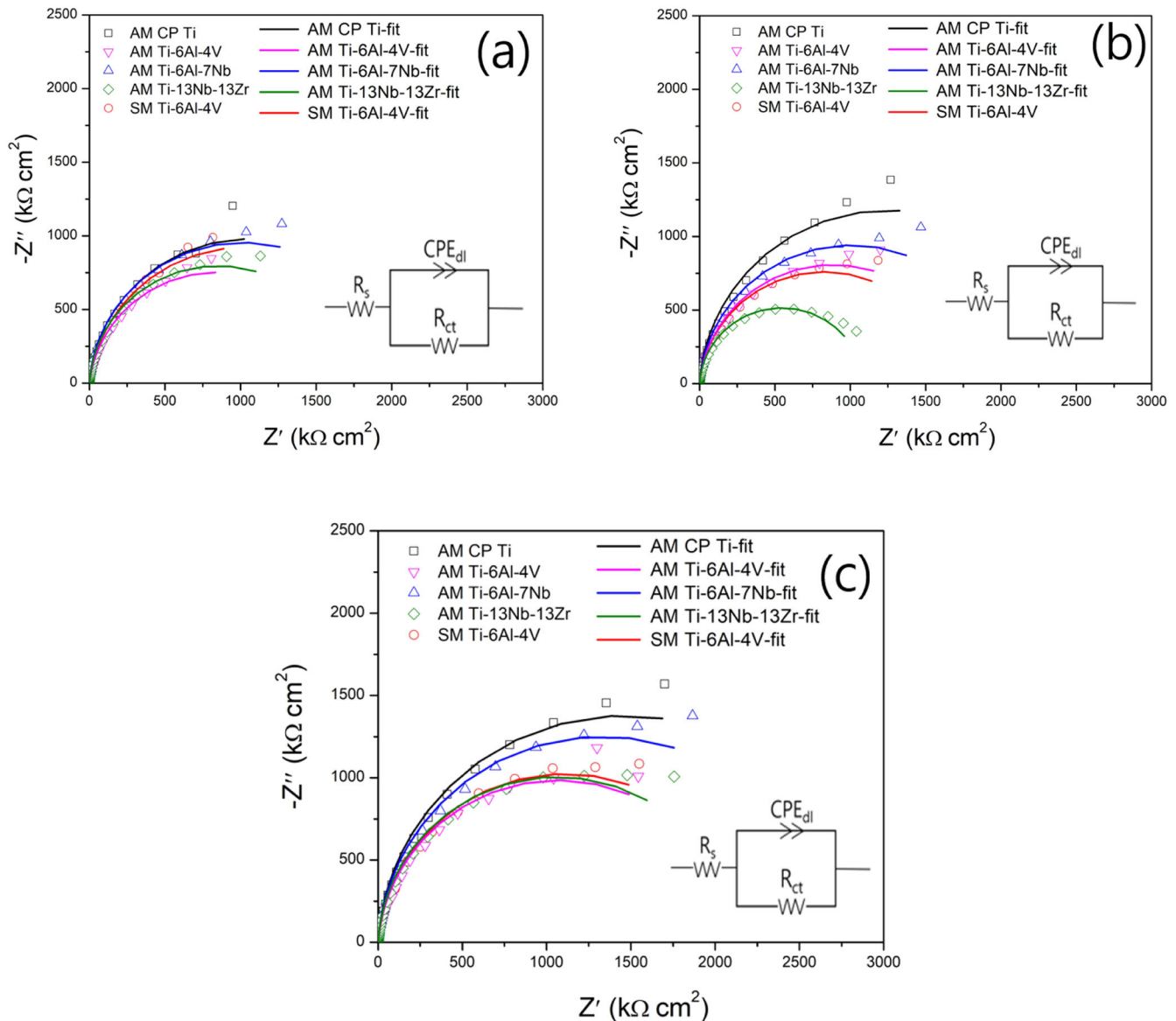


Fig. 2 EIS results represented by the Nyquist plots of SM and AM Ti alloys with the various film formation potentials. **a** 1.0, **b** 1.5, and **c** 2.0 V_{SCE} . The inset equivalent circuit is used to fit impedance spectra.

after the passive film breakdown) was investigated using the abrading electrode technique. Figure 4a shows the current density decay for repassivation with an increase in time on a logarithmic scale. The repassivation kinetics of the SM and AM Ti alloys can be expressed using Eq. (4)³⁷:

$$\log i = \log A - n \log t, \quad (4)$$

where i denotes the anodic current density; A denotes the constant; t denotes the time; n represents the repassivation rate representing the slope of the $\log i - \log t$ plot.

Based on Eq. (4), the value of n is regarded as a repassivation rate of the growth of the passive oxide film on the bare surface. As shown in Fig. 4(b), the repassivation rate (n) consistently decreases in the following order: AM CP Ti, AM Ti-13Nb-13Zr, SM Ti-6Al-4V, AM Ti-6Al-7Nb, and AM Ti-6Al-4V.

E-CLCP studies

Figure 5a, b demonstrates the determination of the E-CLCP in the AM Ti-6Al-4V and AM Ti-6Al-7Nb alloys, respectively. The E-CLCP

of the AM Ti alloy samples was determined by the highest potential value, where there was no further increase in current density in the anodic direction after maintaining a constant potential for 2 h, which is the repassivation potential in the Ringer solution at 37 °C^{31,32}. The E-CLCP values of AM Ti-6Al-4V and AM Ti-6Al-7Nb were measured as 1.544 (± 0.002) V and 1.720 (± 0.007) V, respectively.

Relationship between the resistance to localized corrosion such as pitting, donor density of oxygen vacancies, the diffusion coefficient of oxygen vacancies, and the flux of oxygen vacancies in various AM Ti alloys

Mott-Schottky tests were conducted to investigate the effect of donor densities obtained from Mott-Schottky technique on the pitting potentials measured by potentiodynamic polarization technique. The amounts of donor densities formed on the passive films were measured on the various AM Ti alloys, including CP Ti, Ti-6Al-4V, Ti-6Al-7Nb, Ti-13Nb-13Zr, and SM Ti-6Al-4V. Results show that the AM Ti-6Al-4V alloy with the lowest pitting potential has the lowest donor densities ($6.48 (\pm 0.26) \times 10^{18} \text{ cm}^{-3}$), whereas AM CP Ti ($10.03 (\pm 0.49) \times 10^{18} \text{ cm}^{-3}$) and AM Ti-13Nb-13Zr (11.00

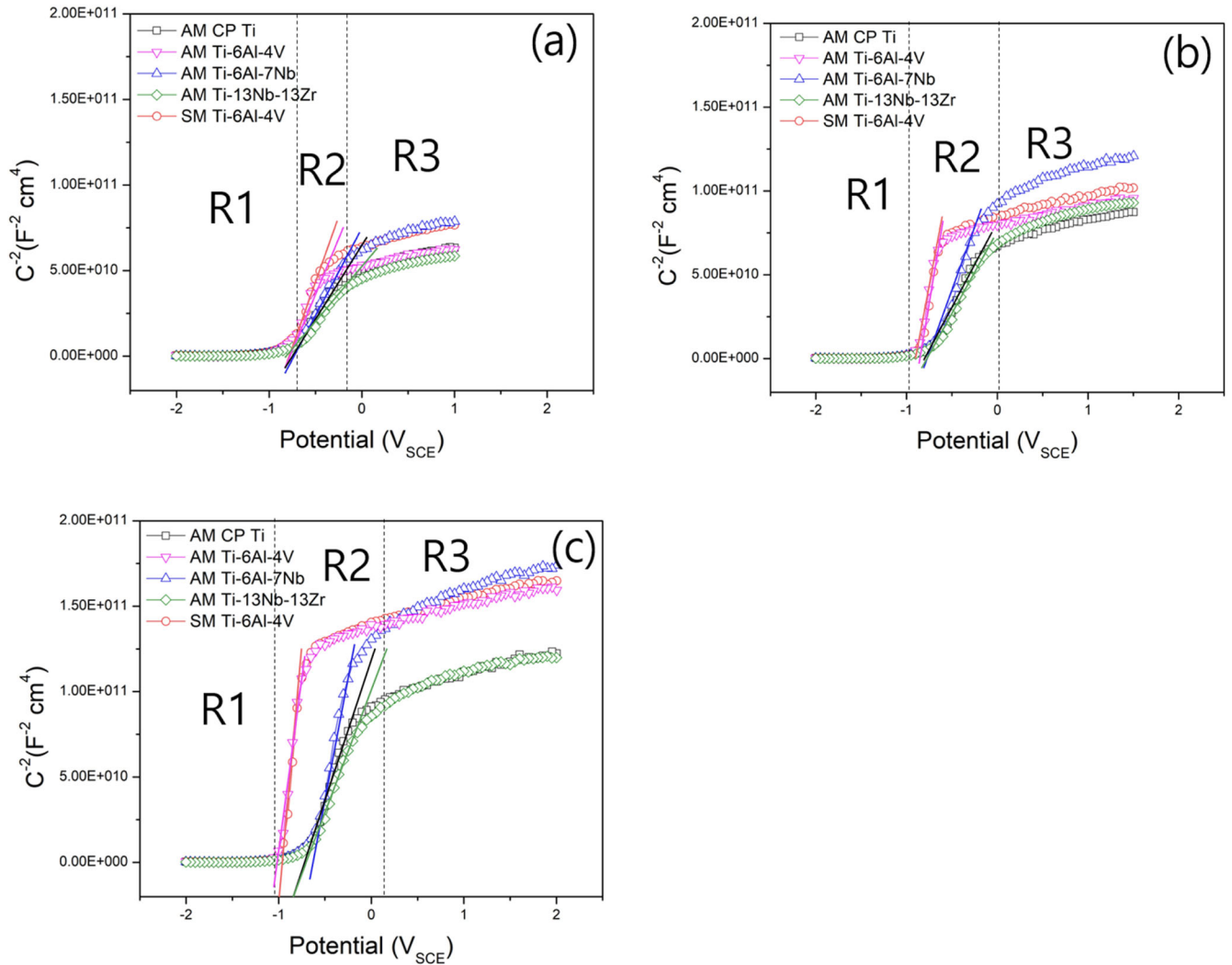


Fig. 3 Mott–Schottky plots for passive films formed on the SM and AM Ti alloys with the film formation potentials of **a** 1.0, **b** 1.5, and **c** 2.0 V_{SCE} .

(± 0.42) $\times 10^{18} \text{ cm}^{-3}$) with more donor densities have higher pitting potentials, indicating better resistance to pitting. These results indicate that donor densities obtained from only Mott–Schottky plots cannot completely explain the results of the resistance to pitting corrosion between various types of AM Ti alloys. Cheng et al. also reported a discrepancy in that Ti–10Mo–6Zr–4Sn–3Nb with more donor densities exhibited higher localized corrosion resistance than Ti–6Al–4V with lower donor densities⁹. Meanwhile, Gai et al.¹¹ studied the flux of oxygen vacancies (J_p) in passive films of SM and AM Ti–6Al–4V alloys in terms of donor densities and diffusion coefficient of oxygen vacancies (D_O) compared with localized corrosion resistances of Ti alloy samples. D_O in the passive film on the SM and AM Ti alloys is determined using Eq. (5)¹²:

$$D_O = \frac{i_p RT}{4eF\varepsilon_L\omega_2}, \quad (5)$$

where i_p represents the current density in the passive state by potentiodynamic polarization technique (noted in Table 1), R represents the ideal gas constant, and F represents Faraday's constant. ε_L denotes the electric field strength in Eq. (7). ω_2 denotes the fitted constant in Eq. (6).

If D_O is high, the outward diffusion of oxygen vacancies in passive films is facilitated and the possibility of reaction with

halogen ions increases on the interfaces between the passive layer and solution.

To obtain ω_2 , N_D (donor densities) is used, as shown in Fig. 6(a). Equation (6) shows the N_D expression with the unknown constants, ω_1 , ω_2 , and b ,

$$N_D = \omega_1 e^{-bE} + \omega_2, \quad (6)$$

where ω_1 , ω_2 , and b represent unknown constants, which are determined by the N_D expression.

As shown in Fig. 6b, ε_L denotes the electric field strength, which is related to applied potential and film thickness, as expressed in Eq. (7)¹²:

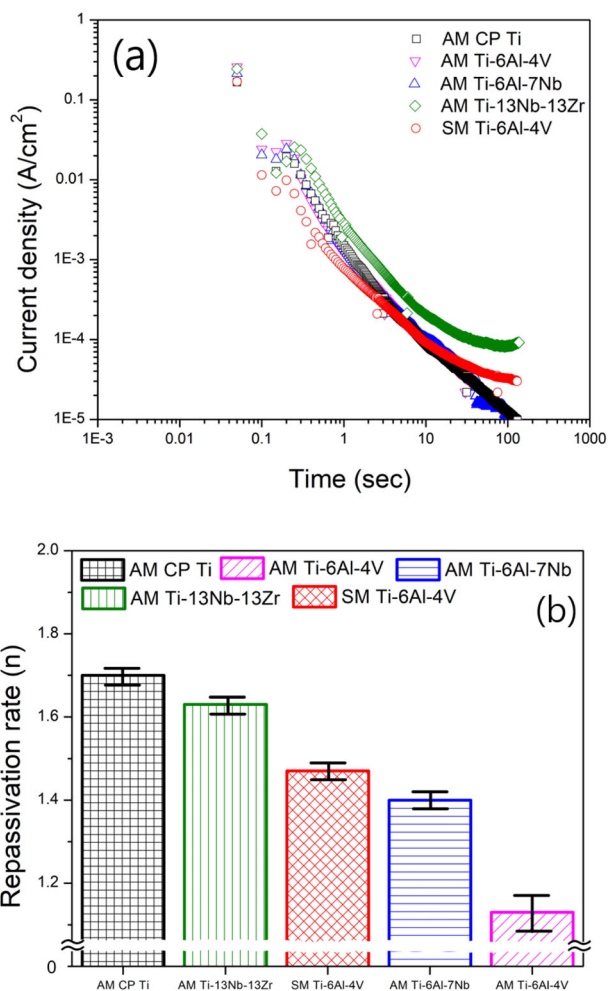
$$d_{\text{eff}} = \frac{(1-\alpha)E}{\varepsilon_L} + B, \quad (7)$$

where α represents surface polarizability with a value of 0.5¹². B represents a constant, and d_{eff} denotes effective film thickness (from Eq. 2).

As mentioned above, D_O is associated with the growth and breakdown of passive films. Higher D_O leads to thicker passive films with higher breakdown susceptibility. As shown in Fig. 7(a), D_O increases in the following order: AM CP Ti, AM Ti–13Nb–13Zr, AM Ti–6Al–7Nb, SM Ti–6Al–4V, and AM Ti–6Al–4V. However, this sequential order does not agree with the tendency of pitting potentials. Therefore, D_O cannot explain the results of the

Table 1. Passive current density, donor density (N_D), diffusion coefficient (D_O), and the flux of vacancies (J_p) of passive films formed on SM and AM Ti alloys at various film formation potentials in Ringer solution at 37 °C.

Film formation potential (V_{SCE})	Passive current density ($\mu A/cm^2$)			Donor density ($10^{18}/cm^3$)			D_O ($10^{-18} m^2/s$)			J_p ($10^{-2} m^2/s$)		
	1.0 V	1.5 V	2.0 V	1.0 V	1.5 V	2.0 V	1.0 V	1.5 V	2.0 V	1.0 V	1.5 V	2.0 V
AM CP Ti	3.853 (± 0.319)	3.999 (± 0.129)	3.454 (± 0.213)	10.03 (± 0.49)	6.57 (± 0.24)	4.55 (± 0.23)	13.9 (± 0.01)	14.5 (± 0.04)	12.4 (± 0.01)	11.0 (± 1.2)	7.64 (± 0.24)	4.57 (± 0.28)
AM Ti-6Al-7Nb	4.549 (± 0.223)	4.946 (± 0.005)	4.732 (± 0.041)	8.44 (± 0.12)	5.00 (± 0.26)	3.20 (± 0.15)	27.8 (± 0.06)	30.2 (± 0.01)	28.9 (± 0.01)	15.7 (± 0.8)	10.1 (± 0.1)	6.21 (± 0.10)
AM Ti-6Al-4V	4.281 (± 0.343)	5.240 (± 0.058)	5.462 (± 0.387)	6.48 (± 0.26)	3.82 (± 0.56)	2.36 (± 0.48)	71.6 (± 0.06)	87.6 (± 0.01)	91.3 (± 0.06)	23.9 (± 1.9)	17.3 (± 0.1)	11.1 (± 0.08)
AM Ti-13Nb-13Zr	5.006 (± 0.490)	5.318 (± 0.646)	5.249 (± 0.648)	11.00 (± 0.42)	7.42 (± 0.31)	5.35 (± 0.22)	14.6 (± 0.02)	15.5 (± 0.02)	15.3 (± 0.02)	11.2 (± 0.8)	7.86 (± 0.9)	5.66 (± 0.61)
SM Ti-6Al-4V	4.346 (± 0.130)	4.561 (± 0.025)	4.521 (± 0.090)	5.26 (± 0.77)	2.96 (± 0.33)	1.83 (± 0.32)	47.1 (± 0.02)	49.4 (± 0.02)	50.0 (± 0.01)	15.4 (± 0.5)	9.12 (± 0.10)	5.59 (± 0.11)

**Fig. 4** Plots of $i(t)$ vs. time in logarithmic scale for **a** SM and AM Ti alloys. **b** Comparison of the repassivation rate obtained from the abrading electrode technique.

resistance to pitting corrosion between various types of AM Ti alloys.

Conversely, the flux of oxygen vacancies (J_p) can be expressed using Eq. (8)¹²:

$$J_p = q_i K D_O N_D, \quad (8)$$

where q_i represents the charge of species ($=2e$), and K is defined as $K = F \epsilon_L / RT$.

J_p values are determined by donor densities (N_D), diffusion coefficient (D_O), and electric field strength (ϵ_L). According to the results of Gai¹¹ high J_p values indicate that passive breakdown can easily occur by facilitating the reaction between oxygen vacancy and halide ion (e.g., Cl^-). Considering the current density at the passive state (i_p), N_D , D_O , and J_p are summarized in Table 1.

As shown in Fig. 7b, the flux of oxygen vacancies (J_p) increases in the following order: AM CP Ti, AM Ti-13Nb-13Zr, SM Ti-6Al-4V, AM Ti-6Al-7Nb, and AM Ti-6Al-4V, which exactly corresponds to the sequential order on pitting potentials determined by potentiodynamic polarization technique. This indicates that the higher the flux of oxygen vacancies, the greater the susceptibility of the passive films of the various Ti alloys to break down. Thus, the resistance to localized corrosion such as pitting among the various Ti alloys is mainly determined by the flux of oxygen vacancies, which is the combination of the donor density and diffusion coefficient of oxygen vacancies.

Repassivation is related to the repassivation kinetics due to the re-formation after the breakdown of a passive film. Repassivation kinetics can be monitored through electrode abrading experiments. According to Eq. (4) ($\log i = \log A - n \log t$), the slope, $-n$ of $\log i$ versus $\log t$ close to 1, is typical for passive films growing without the imposed dissolution of passive films, whereas 0 or positive slopes represent uniform or pitting corrosion, respectively³⁷. The slope of SM and AM Ti alloys greater than 1 indicates the formation of the protective film without the dissolution of passive films. The repassivation slopes of the SM and AM Ti alloys in a biomedical environment decreased in sequential order: AM CP Ti (1.70 (± 0.02)), AM Ti-13Nb-13Zr (1.63 (± 0.02)), SM Ti-6Al-4V (1.47 (± 0.02)), AM Ti-6Al-7Nb (1.40 (± 0.02)), and AM Ti-6Al-4V (1.13 (± 0.04)).

Additionally, Fig. 8 shows that the repassivation rate, the calculated flux of oxygen vacancies, and pitting potentials have the same tendency, indicating that their relationship achieves identical results compared with resistance to localized corrosion between the various AM Ti alloys.

Evaluation of resistance to localized corrosion: survival probability constant

The relationship between repassivation and localized corrosion resistance on the AM Ti alloys is clarified by the introduction of the survival probability constants. To further understand the repassivation mechanism, the PDM proposed by Macdonald²⁷ is examined in terms of the vacancy behavior in the passive film.

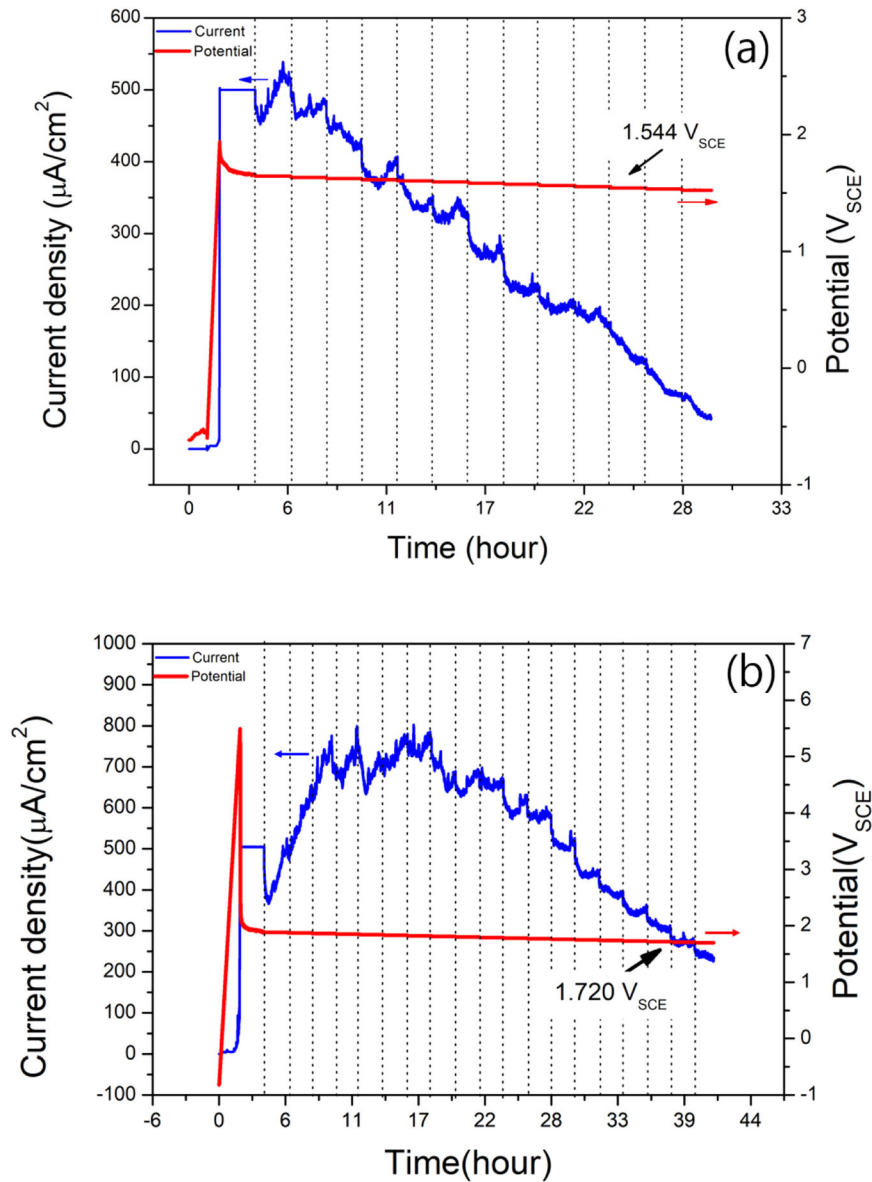
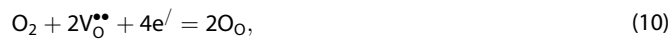


Fig. 5 Determination of E-CLCP values for **a** AM Ti-6Al-4V alloy and **b** AM Ti-6Al-7Nb at 37 °C in Ringer solution.

Application of PDM to AM Ti alloys

According to the application of the PDM to AM Ti alloys, oxygen vacancies are regarded as donors. As shown in Fig. 8, the oxide layer (barrier layer), which is the inner passive film adjacent to the substrate (Ti metal), grows into Ti through the cation-anion-vacancy condensation in Eqs. (9) and (10)³⁸:



where Ti_{Ti} denotes a titanium cation in a normal lattice site and “ \bullet ” and “ \prime ” denote positive and negative charges, respectively.

Oxygen vacancies are generated by the oxidation of Ti^{3+} and Ti^{2+} to Ti^{4+} due to charge compensation. The transport of oxygen vacancies and Ti interstitials and the associated transport of electrons lead to oxide growth.

Oxygen ions diffuse across the oxide layer through their vacancies in the opposite direction, indicated by the arrows in Fig. 9a.

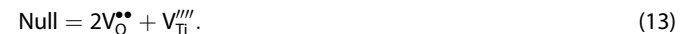
Aggressive ions such as Cl ions diffuse through the hydroxide layer (outer passive layer) adjacent to the solution and subsequently are adsorbed on the oxide surface (Eq. (11)).



where the superscripts “ $-$ ” and “ $*$ ” denote a negative charge and a free site on the oxide surface, respectively. Adsorbed Cl ions (Cl^*) move over the oxide layer. Some of the adsorbed Cl ions will be trapped by oxygen vacancies to form $\text{Cl}_{\text{O}}^{\bullet}$ defects (Eq. (12)).



The system responds to the loss of oxygen vacancies by creating new oxygen vacancies because of charge compensation (Eq. (13), Schottky disorder).



The electric field and the concentration gradient in cation vacancies migrate toward the interface between the metal and barrier layer. Oxygen vacancies at the metal/barrier layer interface will increase with the arrival of cation vacancies to achieve

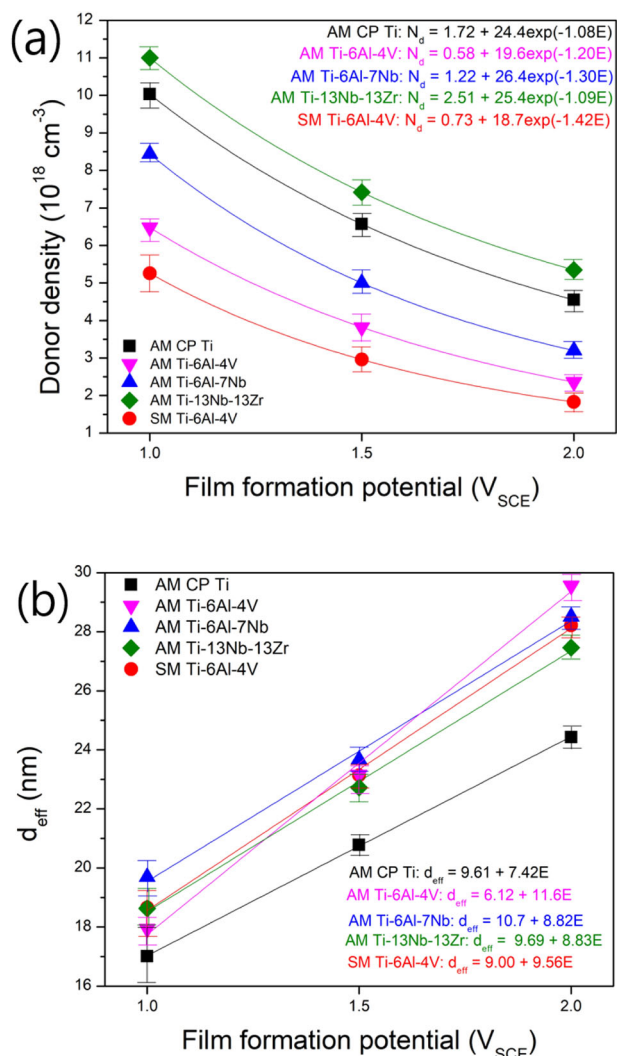


Fig. 6 Semiconductive properties of passive films formed on SM and AM Ti alloys after 2 h potentiostatic polarization at 1.0, 1.5, and 2.0 VSCE. **a** Donor density and **b** thickness of passive films.

electroneutrality. These associations increase with the arrival of more cation vacancies. Eventually, the large association of condensation of vacancies will lead to the formation of voids (void-1, Fig. 9b). These voids locally detach the oxide layer from the metal substrate. The continuous inward oxide growth leads to thinning and subsequent local breakdown of inner passive films through these voids caused by tensile stresses²⁷ (Fig. 9c).

Based on the PDM, the kinetics of pit initiation involves not only the migration of oxygen vacancies but also the generation, migration, and condensation of cation vacancies. The concentration gradient across the oxide layer can be expressed using Fick's first law, and the inward flux of cation vacancies is expressed by Eq. (14)³⁸:

$$J_{V_{\text{Ti}}}^{\text{in}} = \frac{D_{V_{\text{Ti}}}^{\text{in}} [V_{\text{Ti}}^{\text{in}}]}{L}, \quad (14)$$

where $D_{V_{\text{Ti}}}^{\text{in}}$ represents the chemical diffusion/migration coefficient of metal vacancies, and L represents the thickness of the passive film.

Meanwhile, the reaction rate of cation vacancy generation depends exponentially on potential (E) in accordance with the Langmuir isotherm. The dependence of cation vacancy concentration on the Cl^- concentration and electrode potential can be

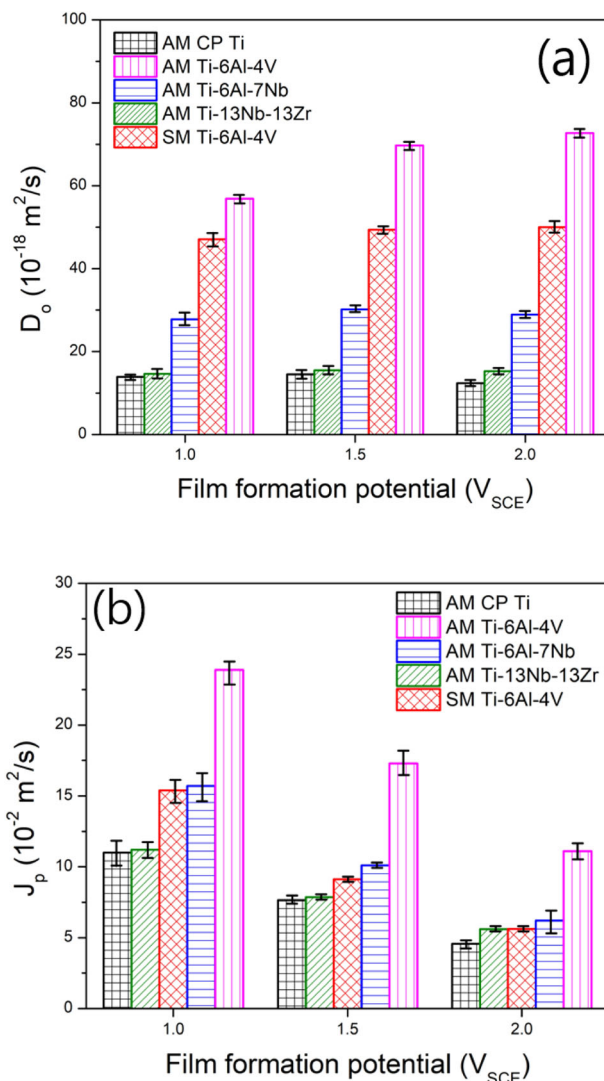


Fig. 7 Semiconductive properties of passive films formed on SM and AM Ti alloys after 2-h potentiostatic polarization at 1.0, 1.5, and 2.0 VSCE. **a** Diffusion coefficient of oxygen vacancy and **b** flux of vacancy.

expressed by Eq. (15)³⁸:

$$[V_{\text{Ti}}^{\text{in}}] = k[\text{Cl}^-]e^{aFE/RT}, \quad (15)$$

where k represents the rate constant for cation vacancy generation.

Therefore, vacancy condensation is proportional to the flux of cation vacancies. Hence, the density of associations or voids (d_{mpit}) can be expressed by Eq. (16)³⁸:

$$d_{\text{mpit}} = kPD_{V_{\text{Ti}}}^{\text{in}}e^{aFE/RT}, \quad (16)$$

where P represents condensation probability.

Most voids repassivate instantaneously after exposure, but a few survive to nucleate stable pits with the survival probability constant (ν). The number of survivable pits is proportional to the void population. When the density of stable pits reaches a critical value, the oxide film can be broken down, and the corresponding potential is the critical pitting potential. Likewise, the critical adsorption of Cl^- concentration (β_{Cl^-}) result in the breakdown of passive films. β_{Cl^-} can be obtained using the nonlinear curve

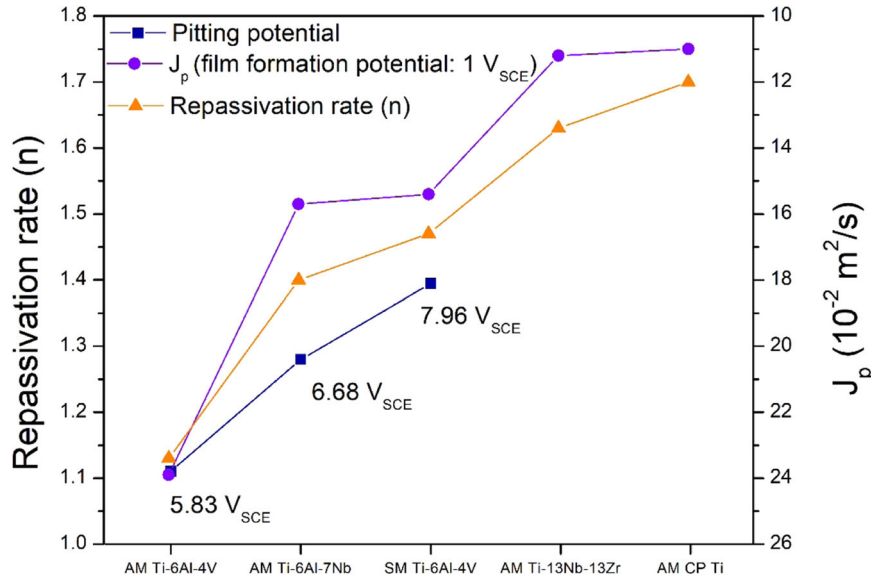


Fig. 8 Comparison of the flux of oxygen vacancy, repassivation rate, and pitting potential of SM and AM Ti alloys.

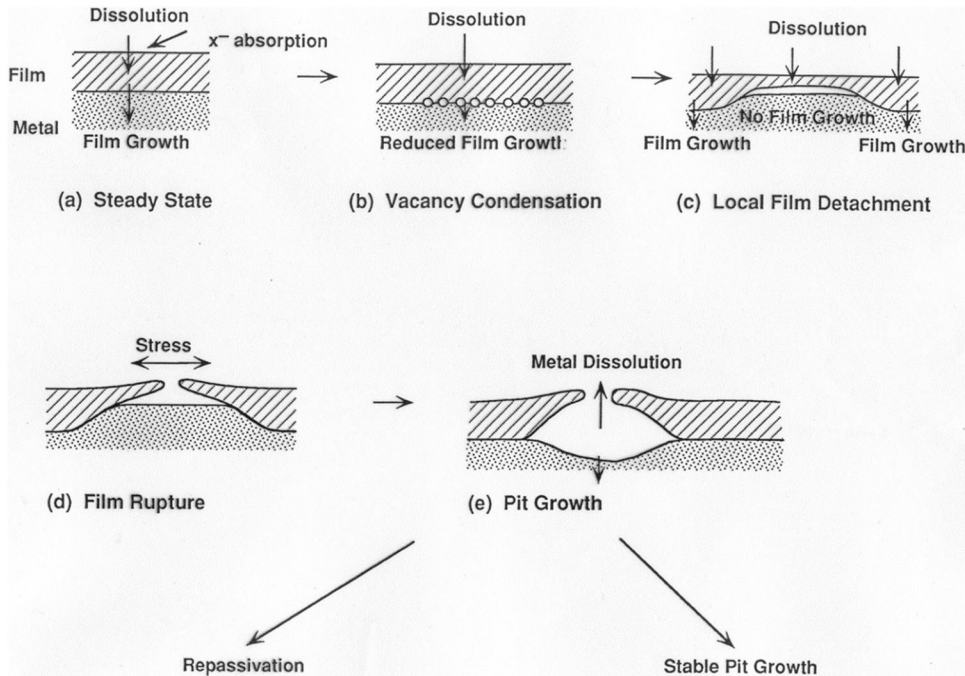


Fig. 9 Schematic illustration of the pit formation on Ti alloys based on the point defect model²⁷.

fitting technique with Eq. (17)³⁹:

$$E_{\text{pit}} = E_{\text{pit}}(r_{\text{Cl}^-}^{\text{sat}}) + \Omega_{\text{Cl}^-} r_{\text{Cl}^-}^{\text{sat}} \left(\frac{1}{1 + \beta_{\text{Cl}^-} [\text{Cl}^-]} \right), \quad (17)$$

where $E_{\text{pit}}(r_{\text{Cl}^-}^{\text{sat}})$ represents the pitting potential when the surface is completely covered by Cl^- , Ω_{Cl^-} denotes a proportionality constant that describes the sensitivity of the pitting potential to the surface concentration of Cl^- , $r_{\text{Cl}^-}^{\text{sat}}$ denotes the surface concentration of Cl^- , β_{Cl^-} denotes the equilibrium adsorption coefficient of Cl^- , and $[\text{Cl}^-]$ is mole concentration of Cl^- .

Survival probability constants of AM Ti alloys

Figure 10 exhibits the pitting potential of AM Ti-6Al-7Nb and AM Ti-6Al-4V at various Cl concentrations, respectively. According to

the nonlinear curve fitting results in terms of $E_{\text{pit}}(r_{\text{Cl}^-}^{\text{sat}})$, the pitting potentials measured in saturated NaCl are 5.26 and 4.46 V in AM Ti-6Al-7Nb and AM Ti-6Al-4V, respectively. AM Ti-6Al-7Nb and AM Ti-6Al-4V have $\Omega_{\text{Cl}^-} r_{\text{Cl}^-}^{\text{sat}}$ values of 2.05 and 13.8 V, respectively. Using the nonlinear curve fitting technique, the equilibrium adsorption coefficient of Cl^- of AM Ti-6Al-7Nb and AM Ti-6Al-4V, that is, β_{Cl^-} , are calculated as 2.94 and 60.6 M⁻¹, respectively. This means that chloride ions are easier to adsorb on the surface of AM Ti-6Al-4V than on that of AM Ti-6Al-7Nb. The adsorption coefficient obtained by Eq. (17) and the survival probability constant (ν) are related in Eq. (18)³⁸:

$$E_{\text{pit}} = -\frac{RT}{\alpha F} \ln \frac{1}{\beta_{\text{Cl}^-}} + \frac{1}{\alpha} \ln \frac{\nu d_{\text{mpit}}}{kPD_{\text{V}_{\text{Ti}}}}. \quad (18)$$

Lee and Seo^{32,33} measured E-CLCP values as repassivation potentials of AM Ti alloys using a new localized corrosion resistance test method for AM Ti alloys. As shown in Fig. 5, the AM Ti-6Al-4V and AM Ti-6Al-7Nb alloys have E-CLCP values of 1.544 and 1.720 V_{SCE}, respectively. If the potential (E) of Eq. (16) is replaced with the E-CLCP, survival probability constants can be calculated using the following equation:

$$v = e^{\alpha(E_{\text{pit}} + \frac{RT}{\alpha F} \ln \frac{1}{K_{\text{Cl}}} - \frac{E_{\text{CLCP}}}{RT})} \quad (19)$$

The survival probability constants, v values obtained from Eq. (19), are 2.81×10^{-13} and 4.62×10^{-12} for AM Ti-6Al-7Nb and AM Ti-6Al-4V, respectively, whereas those of stainless steels are $\sim 10^{-2}$ – 10^{-5} ⁴⁰ indicating that Ti alloys have significantly greater localized corrosion resistance than stainless steels. Because of its lower repassivation properties, AM Ti-6Al-4V has higher survival probability constants than AM Ti-6Al-7Nb. This means that AM Ti-6Al-4V is easier to transition from metastable pits to stable pits than AM Ti-6Al-7Nb, resulting in a higher survival probability constant. Repassivation kinetics of AM Ti alloys is represented by the survival probability constant, indicating that the higher the survival probability constant, the easier the occurrence of localized corrosion.

The resistance to localized corrosion and repassivation for SM Ti-6Al-4V and AM Ti alloys including AM Ti-6Al-4V are studied. The localized corrosion resistance is mainly determined by the flux of oxygen vacancies, which comprises the donor density and diffusion coefficient of oxygen vacancies. It is found that localized corrosion resistances of various AM Ti alloys is determined by the flux of oxygen vacancies rather than the amount of donor density. The repassivation kinetics of AM Ti alloys is analyzed by the survival probability constant based upon PDM. Since generated oxygen vacancies and accumulated cation vacancies affect the occurrence on the localized corrosion, the increase in oxygen and

cation vacancies can result in the more stable pits. As a result, the higher the survival probability constant, the easier the transition of metastable pits to stable pits, the more difficult repassivation and finally the easier occurrence of localized corrosion. The accurate role of alloying elements may be also important in AM Ti alloys containing precipitates due to alloying elements. The precipitates such as Ti₃Al or TiAl may represent the deteriorated resistances to localized corrosion, on the contrary, make the beneficial effect on those due to the accelerated repassivation. In some case the precipitates may play an important role on repassivation in mild corrosive environments such as simulated human body conditions while in harsh environments such as 25% NaCl aqueous solution, the precipitates may provide the initiation site for localized corrosion instead of repassivation³³.

METHODS

Samples and test solution preparation

SM and AM Ti alloys, including AM CP Ti, AM Ti-6Al-4V, AM Ti-6Al-7Nb, AM Ti-13Nb-13Zr, and SM Ti-6Al-4V alloys, were used as samples. The exposed area of the samples was approximately 1.0 cm² in the electrolyte. AM Ti samples were manufactured through the DED process (InssTek, Korea) with a laser power of 460 W and a laser scan speed of 0.85 m/min under Ar gas conditions. Table 2 shows the weight composition of powder percentage of all test samples. All fabricated samples were wet-ground to 600-grit SiC paper, washed using double-distilled water, and air-dried. Before the electrochemical tests, a deaerated Ringer solution (8.69 g/L NaCl, 0.30 g/L KCl, and 0.48 g/L CaCl₂)³⁵ was prepared at a temperature of 37 °C.

Microstructural characterization

The sample surfaces were etched using a solution of Kroll's reagent containing 10 mL HNO₃, 5 mL HF, and 85 mL H₂O for 10 s. Field emission-scanning electron microscopy (FE-SEM) was performed using JEOL JSM-7610F equipped with a retractable backscattered-electron detector to characterize all etched samples.

The phase was identified through X-ray diffraction (XRD) using a Rigaku D/MAX 2500/PC fitted with a Cu-K α radiation source. The samples were scanned at room temperature when $2\theta = 30^\circ$ – 90° with a step size of 1° and a dwell time of 1 min per step. The JADE9 (KSAAnalyst) software was used to analyze the XRD pattern results.

Electrochemical measurements

A Gamry PCB-4750 potentiostat was used for electrochemical measurements. A three-electrode system was used. The platinum wire was used as the counter electrode. A saturated calomel electrode (SCE) was used to facilitate the potential measurements. Samples mounted by flat cell in 1.0 cm². Additionally, a Luggin probe was used to connect the reference and working electrodes.

Potentiodynamic polarization tests were conducted at a potential of -200 mV below the open-circuit potential, up to 9.0 V, or the pitting potential at a scan rate of 1 mV/s.

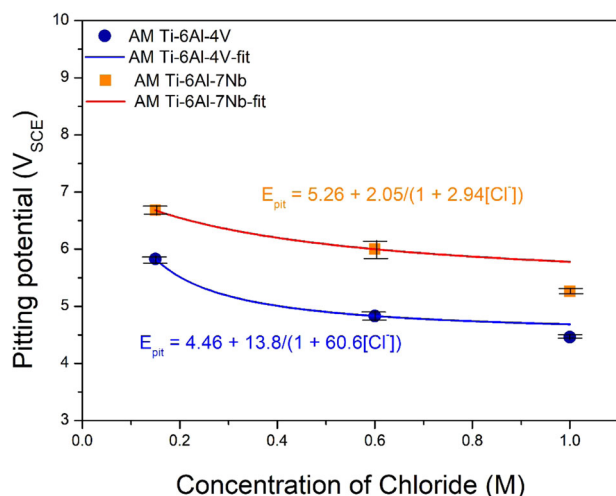


Fig. 10 Epit of AM Ti-6Al-7Nb and AM Ti-6Al-4V as a function of the concentration of NaCl. The solid lines correspond to Eq. (17).

Table 2. Material composition of SM and AM Ti alloys (wt%).

	C	Fe	Al	V	Sn	Nb	O	N	H	Zr	Ti
AM CP Ti	0.1	0.3	-	-	-	-	-	0.03	0.015	-	Bal.
AM Ti-6Al-7Nb	0.01	0.125	6.05	-	-	7.1	0.1	0.01	0.001	-	Bal.
AM Ti-6Al-4V	0.011	0.18	6.1	3.7	0.01	-	-	-	-	-	Bal.
AM Ti-13Nb-13Zr	0.015	0.001	-	-	-	13.8	0.09	0.01	0.002	12.7	Bal.
SM Ti-6Al-4V	0.04	0.16	5.9	4.1	-	-	0.15	-	0.001	-	Bal.

The samples were statically polarized for 2 h during the formation of passive films for Mott–Schottky and EIS measurements at the film formation potentials of 1.0, 1.5, or 2.0 V.

The EIS measurements at the various film formation potentials (1.0, 1.5, or 2.0 V) were potentiostatically conducted at an alternating current voltage amplitude of 10 mV within the frequency range of 10^{-2} – 10^5 Hz. The EIS results were analyzed using the Gamry Echem Analyst software.

Capacitance was measured at 1000 Hz using a potentiostat. Polarization was applied at successive steps of 50 mV, starting at the film formation potentials (1.0, 1.5, or 2.0 V) in the cathodic direction up to -2.0 V.

An abrading electrode technique was used to obtain the repassivation kinetics of oxide films on the samples after exposure of their bare surfaces to the solution³⁷. The electrode was abraded with a 2000-grit SiC disc while immersed in the electrolyte to acquire current transients. The sample was mounted in the center of an epoxy resin with an exposed area of 0.18 cm² welded with copper wire. The sample surface was renewed by abrading with a 2000-grit SiC disc fixed to the rotating shaft operated by a direct current motor. A carbon rod was used as the counter electrode, and an SCE was used as the reference electrode. The resulting current transient was acquired at an applied potentiostatic potential of 1.0 V in the passive potential region of SM and AM Ti alloys according to potentiodynamic polarization curves.

All electrochemical measurements were performed in triplicate to ensure data reproducibility.

E-CLCP measurements

E-CLCP values were obtained by measuring the repassivation potential through potentiodynamic–galvanostatic–potentiostatic processes. E-CLCP was determined in accordance with the following steps proposed by Lee and Seo^{32,33}:

The test sample was prepared without a crevice former. Potentiodynamic anodic polarization was performed from an open-circuit potential until the anodic current density rose to 500 μ A/cm² at 1 mV/s potential sweep velocity using a potentiostat. When the anodic current density reached 500 μ A/cm², it was immediately maintained for 2 h. After holding the constant current density of 500 μ A/cm² for 2 h, a constant polarization was immediately maintained in the reverse (cathodic) direction at an electrode potential of 10 mV, which was lower than the initial potential. Immediately, an increase in current density was observed in the anodic direction, the constant potential was further decreased by 10 mV. This operation was repeated until no further increase in current density was found in the anodic direction after maintaining a constant potential for 2 h. The E-CLCP of AM Ti alloy specimens was determined at the highest potential value, where no further increase in current density was found in the anodic direction after maintaining a constant potential for 2 h.

All electrochemical measurements were performed in triplicate to ensure data reproducibility.

DATA AVAILABILITY

Data sharing is not applicable to this article as no datasets were generated or analyzed during the current study.

Received: 11 October 2022; Accepted: 12 May 2023;

Published online: 26 May 2023

REFERENCES

- Boyer, R.; Welsch, G.; Collings, E. W. *Materials Properties Handbook: Titanium Alloys*, ASM International, Materials Park, OH, 1994.
- Kruth, J. P., Levy, G., Klocke, F. & Childs, T. H. C. Consolidation phenomena in laser and powder-bed based layered manufacturing. *CIRP Ann.* **56**, 730–759 (2007).
- Shukla, A. K., Balasubramaniam, R. & Bhargava, S. Properties of passive film formed on CP titanium, Ti-6Al-4V and Ti-13.4 Al-29Nb alloys in simulated human body conditions. *Intermetallics* **13**, 631–637 (2005).
- Qin, P. et al. Resemblance in corrosion behavior of selective laser melted and traditional monolithic β Ti-24Nb-4Zr-8Sn alloy. *ACS Biomater. Sci. Eng.* **5**, 1141–1149 (2019).
- Cremaşco, A., Osório, W. R., Freire, C. M. A., Garcia, A. & Caram, R. Electrochemical corrosion behavior of a Ti-35Nb alloy for medical prostheses. *Electrochim. Acta* **53**, 4867–4874 (2008).
- Mareci, D., Sutiman, D., Chelariu, R., Leon, F. & Curteanu, S. Evaluation of the corrosion resistance of new ZrTi alloys by experiment and simulation with an adaptive instance-based regression model. *Corros. Sci.* **73**, 106–122 (2013).
- Krewski, D. et al. Human health risk assessment for aluminium, aluminium oxide, and aluminium hydroxide. *J. Toxicol. Environ. Health B Crit. Rev.* **10**, 1–269 (2007).
- Zhang, L. C. & Chen, L. Y. A review on biomedical titanium alloys: recent progress and prospect. *Adv. Eng. Mater.* **21**, 1801215 (2019).
- Cheng, J. et al. Corrosion behavior of as-cast Ti-10Mo-6Zr-4Sn-3Nb and Ti-6Al-4V in Hank's solution: a comparison investigation. *Metals* **11**, 11–26 (2021).
- Horn, T. J. & Harrysson, O. L. Overview of current additive manufacturing technologies and selected applications. *Sci. Prog.* **95**, 255–282 (2012).
- Liu, S. & Shin, Y. C. Additive manufacturing of Ti6Al4V alloy: a review. *Mater. Des.* **164**, 107552 (2019).
- Gai, X. et al. Electrochemical behaviour of passive film formed on the surface of Ti-6Al-4V alloys fabricated by electron beam melting. *Corros. Sci.* **145**, 80–89 (2018).
- Wauthle, R. et al. Effects of build orientation and heat treatment on the microstructure and mechanical properties of selective laser melted Ti6Al4V lattice structures. *Addit. Manuf.* **5**, 77–84 (2015).
- Yadroitsev, I., Krakhmalev, P. & Yadroitsava, I. Selective laser melting of Ti6Al4V alloy for biomedical applications: temperature monitoring and microstructural evolution. *J. Alloy. Compd.* **583**, 404–409 (2014).
- Vrancken, B., Thijs, L., Kruth, J. P. & Van Humbeeck, J. V. Heat treatment of Ti6Al4V produced by selective laser melting: microstructure and mechanical properties. *J. Alloy. Compd.* **541**, 177–185 (2012).
- Dai, N., Zhang, L. C., Zhang, J., Chen, Q. & Wu, M. Corrosion behavior of selective laser melted Ti-6Al-4 V alloy in NaCl solution. *Corros. Sci.* **102**, 484–489 (2016).
- Casadebaigt, A., Hugues, J. & Monceau, D. Influence of microstructure and surface roughness on oxidation kinetics at 500–600 °C of Ti-6Al-4V alloy fabricated by additive manufacturing. *Oxid. Met.* **90**, 633–648 (2018).
- Tamilselvi, S., Raman, V. & Rajendran, N. Corrosion behaviour of Ti-6Al-7Nb and Ti-6Al-4V ELI alloys in the simulated body fluid solution by electrochemical impedance spectroscopy. *Electrochim. Acta* **52**, 839–846 (2006).
- Zhang, L. C. & Attar, H. Selective laser melting of titanium alloys and titanium matrix composites for biomedical applications: a review. *Adv. Eng. Mater.* **18**, 463–475 (2016).
- Dai, N. et al. Distinction in corrosion resistance of selective laser melted Ti-6Al-4V alloy on different planes. *Corros. Sci.* **111**, 703–710 (2016).
- Seo, D. I. & Lee, J. B. Corrosion characteristics of additive-manufactured Ti-6Al-4V using microdroplet cell and critical pitting temperature techniques. *J. Electrochem. Soc.* **166**, C428–C433 (2019).
- Seo, D. I. & Lee, J. B. Effects of competitive anion adsorption (Br⁻ or Cl⁻) and semiconducting properties of the passive films on the corrosion behavior of the additively manufactured Ti-6Al-4V alloys. *Corros. Sci.* **173**, 108789 (2020).
- Seo, D. I. & Lee, J. B. Influence of heat treatment parameters on the corrosion resistance of additively manufactured Ti-6Al-4V alloy. *J. Electrochem. Soc.* **167**, 101509 (2020).
- Lee, J. B., Seo, D. I. & Chang, H. Y. Evaluating corrosion resistance of additive-manufactured Ti-6Al-4V using electrochemical critical localized corrosion temperature. *Met. Mater. Int.* **26**, 39–45 (2020).
- Qin, P. et al. Corrosion and passivation behavior of laser powder bed fusion produced Ti-6Al-4V in static/dynamic NaCl solutions with different concentrations. *Corros. Sci.* **191**, 109728 (2021).
- Chen, L. Y. et al. Corrosion behavior and characteristics of passive films of laser powder bed fusion produced Ti-6Al-4V in dynamic Hank's solution. *Mater. Des.* **208**, 109907 (2021).
- Macdonald, D. D. The point defect model for the passive state. *J. Electrochem. Soc.* **139**, 3434–3449 (1992).
- Roh, B. & Macdonald, D. D. Passivity of titanium: part II, the defect structure of the anodic oxide film. *J. Solid State Electrochem* **23**, 1967–1979 (2019).
- Roh, B. & Macdonald, D. D. Passivity of titanium: part IV, reversible oxygen vacancy generation/annihilation. *J. Solid State Electrochem* **23**, 2863–2879 (2019).

30. Yu, J., Zhao, Z. J. & Li, L. X. Corrosion fatigue resistances of surgical implant stainless steels and titanium alloy. *Corros. Sci.* **35**, 587–597 (1993).
31. Bundy, K. J., Marek, M. & Hochman, R. F. In vivo and in vitro studies of the stress-corrosion cracking behavior of surgical implant alloys. *J. Biomed. Mater. Res.*, **17**, 467–487 (1983).
32. Lee, J. B., Seo, D. I. & Chang, H. Y. Correction to: Evaluating corrosion resistance of biomedical Ti 6Al 4V alloys fabricated via additive manufacturing using electrochemical critical localized corrosion potential. *Met. Mater. Int.* **27**, 3095–3095 (2021).
33. Seo, D. I. & Lee, J. B. Localized corrosion resistance on additively manufactured Ti alloys by means of electrochemical critical localized corrosion potential in biomedical solution environments. *Materials* **14**, 7481 (2021).
34. Brug, G. J., van den Eeden, A. L. G., Sluyters-Rehbach, M. & Sluyters, J. H. The analysis of electrode impedances complicated by the presence of a constant phase element. *J. Electroanal. Chem.* **176**, 275–295 (1984).
35. Schmidt, A. M., Azambuja, D. S. & Martini, E. M. A. Semiconductive properties of titanium anodic oxide films in McIlvaine buffer solution. *Corros. Sci.* **48**, 2901–2912 (2006).
36. Lee, J. B. & Yoon, S. I. Effect of nitrogen alloying on the semiconducting properties of passive films and metastable pitting susceptibility of 316L and 316LN stainless steels. *Mater. Chem. Phys.* **122**, 194–199 (2010).
37. Lee, J. B. Effects of alloying elements, Cr, Mo and N on repassivation characteristics of stainless steels using the abrading electrode technique. *Mater. Chem. Phys.* **99**, 224–234 (2006).
38. Jiang, Z., Dai, X., Norby, T. & Middleton, H. Investigation of pitting resistance of titanium based on a modified point defect model. *Corros. Sci.* **53**, 815–821 (2011).
39. Basame, S. B. & White, H. S. Pitting corrosion of titanium the relationship between pitting potential and competitive anion adsorption at the oxide film/electrolyte interface. *J. Electrochem. Soc.* **147**, 1376–1381 (2000).
40. Williams, D. E., Stewart, J. & Balkwill, P. H. The nucleation, growth and stability of micropits in stainless steel. *Corros. Sci.* **36**, 1213–1235 (1994).

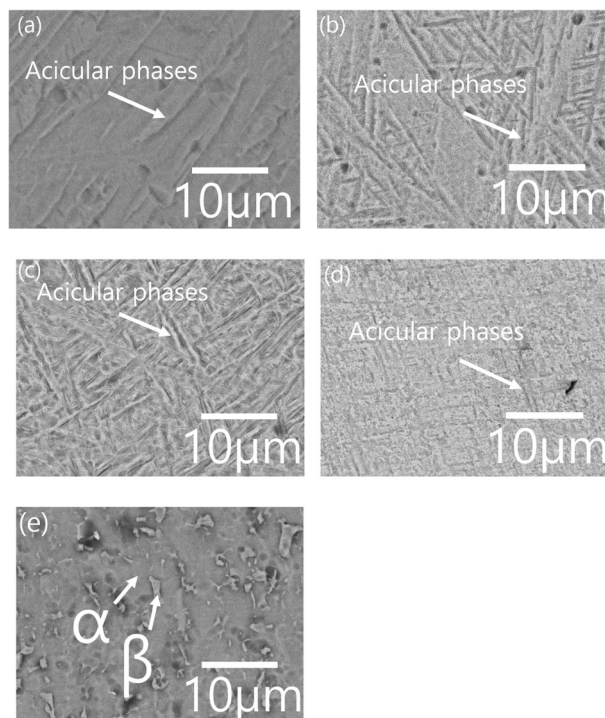


Fig. 11 FE-SEM micrographs of SM and AM Ti alloys. **a** AM CP Ti, **b** AM Ti–6Al–7Nb, **c** AM Ti–6Al–4V, **d** AM Ti–13Nb–13Zr, and **e** SM Ti–6Al–4V.

ACKNOWLEDGEMENTS

This work was supported by the Technology Innovation Program (20006868, Standard Development for Corrosion testing of additively manufactured (3D Printing) Bio-metallic material), which is funded By the Ministry of Trade, Industry, & Energy (MOTIE, Korea).

AUTHOR CONTRIBUTIONS

J.-B.L.: Conceptualization, Methodology, Resources, Writing—review & editing, Supervision, Project administration, Funding acquisition. D.-I.S.: Investigation, Data curation, Software, Writing—original draft, Visualization.

COMPETING INTERESTS

The authors declare no competing interests.

APPENDIX A: MICROSTRUCTURE STUDIES

Figure 11a–d shows the micrographs of AM CP Ti, AM Ti–6Al–4V, AM Ti–6Al–7Nb, and AM Ti–13Nb–13Zr alloys based on FE-SEM, respectively. As shown in Fig. 11(e), SM Ti–6Al–4V alloys have both α and β phases whereas, AM Ti alloys have grains with acicular martensite α' .

Figure 12 shows the XRD results of the SM and AM Ti samples, indicating that SM Ti–6Al–4V only displays α and β phases as the (110) plane, whereas the phases of AM Ti alloys comprise only α and α' phases without any β phase.

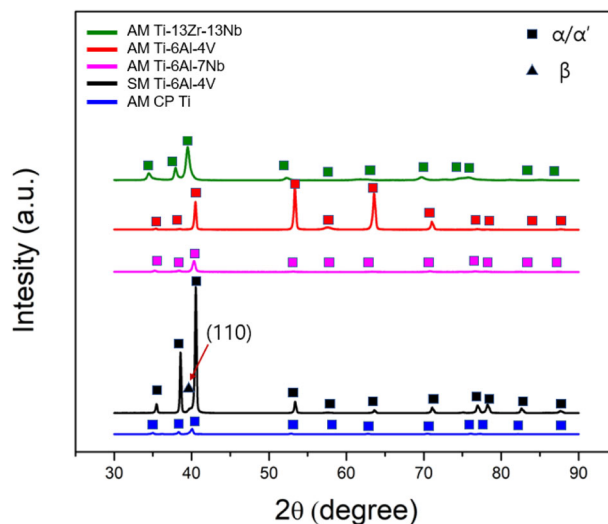


Fig. 12 XRD patterns of SM and AM Ti alloys.

ADDITIONAL INFORMATION

Correspondence and requests for materials should be addressed to Jae-Bong Lee.

Reprints and permission information is available at <http://www.nature.com/reprints>

Publisher's note Springer Nature remains neutral with regard to jurisdictional claims in published maps and institutional affiliations.



Open Access This article is licensed under a Creative Commons Attribution 4.0 International License, which permits use, sharing, adaptation, distribution and reproduction in any medium or format, as long as you give appropriate credit to the original author(s) and the source, provide a link to the Creative Commons license, and indicate if changes were made. The images or other third party material in this article are included in the article's Creative Commons license, unless indicated otherwise in a credit line to the material. If material is not included in the article's Creative Commons license and your intended use is not permitted by statutory regulation or exceeds the permitted use, you will need to obtain permission directly from the copyright holder. To view a copy of this license, visit <http://creativecommons.org/licenses/by/4.0/>.

© The Author(s) 2023